

Article

Enhanced Gas Sensing Performance of CuO-ZnO Composite Nanostructures for Low-Concentration NO₂ Detection

Hakimeh Pakdel , Matteo Borsi, Massimo Ponzoni and Elisabetta Comini * 

Sensor Laboratory, Department of Information Engineering, University of Brescia, Via Valotti 9, 25133 Brescia, Italy; h.pakdel@unibs.it (H.P.); matteo.borsi@unibs.it (M.B.); massimo.ponzoni@unibs.it (M.P.)
* Correspondence: elisabetta.comini@unibs.it

Abstract: The detection of nitrogen dioxide (NO₂) is essential for safeguarding human health and addressing environmental sustainability. That is why, in the last decades, gas sensors have been developed to detect NO₂ to overcome these hazards. This study explores the use of a novel CuO-ZnO composite synthesized through a polyol and sol-gel technique to enhance gas sensing performance. The CuO-ZnO composite offers the advantage of a synergic combination of its properties, leading to improved sensitivity, selectivity, and low detection limit. The innovative polyol technique employed in this research enables the controlled synthesis of hierarchical CuO and porous ZnO structures. The composite formation is achieved using the sol-gel method, resulting in CuO-ZnO composites with different ratios. The structural, morphological, and optical properties of the materials have been characterized using FESEM, X-ray diffraction, and UV-vis spectroscopy. Gas sensing experiments demonstrate enhanced performance, particularly in sensitivity and selectivity for NO₂, even at low concentrations. The composites also exhibit improved baseline stability compared to pristine CuO and ZnO. This study explains the influence of humidity on gas sensing properties by examining interactions between water molecules and sensor surfaces. Notably, the developed CuO-ZnO composite displays excellent selectivity towards NO₂, attributed to favorable bonding characteristics and acid-base properties. Overall, this research contributes to advancing gas sensor technology, providing a promising potential for sensitive and selective NO₂ detection, thereby addressing critical needs for human health and environmental protection.



Citation: Pakdel, H.; Borsi, M.; Ponzoni, M.; Comini, E. Enhanced Gas Sensing Performance of CuO-ZnO Composite Nanostructures for Low-Concentration NO₂ Detection. *Chemosensors* **2024**, *12*, 54. <https://doi.org/10.3390/chemosensors12040054>

Academic Editor: Fanli Meng

Received: 19 February 2024

Revised: 26 March 2024

Accepted: 3 April 2024

Published: 5 April 2024



Copyright: © 2024 by the authors. Licensee MDPI, Basel, Switzerland. This article is an open access article distributed under the terms and conditions of the Creative Commons Attribution (CC BY) license (<https://creativecommons.org/licenses/by/4.0/>).

Keywords: CuO-ZnO composite; NO₂; gas sensor; gas sensing performance; selectivity

1. Introduction

Toxic gases and volatile compounds (VOCs) could be harmful to human health in a short time and lead to climate change and global warming in the long term [1–3]. Among these hazardous gases, nitrogen dioxide (NO₂) as a major component of NO_x gases plays a significant role in the formation of ground-level ozone and contributes to producing some harmful chemical compounds and acid rain [4,5]. Short-term exposure to NO₂ can lead to breathing issues, such as coughing, and wheezing, while prolonged exposure to high concentrations of NO₂ levels can cause severe respiratory infections [6–8]. Furthermore, children and elderly people with asthma are particularly vulnerable to NO₂ exposure [9,10]. Studies have demonstrated a correlation between NO₂ concentrations in different cities and an increase in COVID-19 cases [11]. Hence, given the hazardous effects of NO₂ on human health and the environment, detecting it below the threshold limit is critical. Some research has focused on monitoring and reducing environmental pollution by developing sensors for low concentrations of NO₂ detection following the use of novel catalysts to convert NO₂ into harmless gaseous species [12–14].

Different materials including polymers, carbon, and semiconductor nanomaterials have been employed for gas detection [15]. Among these different nanomaterials, metal oxide gas sensors have attracted much attention in recent years due to their applicability,

ranging from health and safety (including food processing, air quality monitoring, and breath analysis) to energy efficiency and emission control in combustion processes [16,17]. In addition, gas sensor-based metal oxide nanostructures have exhibited various advantages, including their high sensitivity, simplicity, low cost, and simple integration [18]. However, the metal oxide gas sensing devices show poor chemical selectivity due to resistance changes when exposed to other gaseous species. Thus, by combining sensing materials through doping, composite preparation, and surface modification, researchers have enhanced gas sensing performance factors, such as selectivity, gas sensing response, recovery, and response time [19].

Copper oxide (CuO), a p-type semiconductor metal oxide with a narrow band gap (1.2 eV), has been extensively studied in applications, including electronics, batteries, solar energy devices, and gas sensors. Copper oxide's high catalytic activity, good thermal stability, adjustable surface, and non-toxicity make it an ideal material for these applications [20]. However, it has not been widely used compared to some n-type semiconductor gas sensing materials, like SnO₂, ZnO, In₂O₃, and TiO₂ [21]. Nevertheless, some research has reported good sensitivity of CuO-based sensors towards NO₂ [22,23]. On the other hand, zinc oxide (ZnO) is an n-type semiconductor with a wide band gap (3.37 eV) and has become the most widely sensing material for the detection of NO₂ owing to its good chemical stability and electrical and non-toxic properties [24]. To improve the gas sensing performance of the CuO nanostructure, such as sensitivity and selectivity, CuO-ZnO composites were synthesized in this study using a two-step preparation method without using structure-directing agents. Previous research with a similar focus has predominantly employed various methods, precursors, reaction conditions, and sometimes toxic additives, such as HCl, oxalic acid, and sodium sulfate, as well as different structure-directing agents. However, some methods are not cost-effective and require complex instrumentation [25,26]. Our study introduces a simple and low-cost approach to synthesizing CuO-ZnO composites using a polyol and sol-gel technique.

The innovative polyol technique presents a novel approach to achieve chemical processes at low temperatures. This method was first developed to synthesize sub-micron metal powder [27]. The preparation involves dissolving suitable solid metal salts in a liquid polyol. The prepared suspension was stirred and heated. This controlled reduction process leads to the formation of metal powders. The polyol liquid serves not only as a solvent but also as a capping agent, preventing undesirable particle growth and agglomeration [28]. More recently, this technique has been extended to the synthesis of metal oxides and metal chalcogenides, expanding its applicability [29]. Thus, in this study, ethylene glycol (EG) acts as both solvent and capping agent to control shape and crystallization formation in preparation of bare metal oxide. This efficient method produces a hierarchical CuO and porous ZnO structure.

2. Materials and Methods

2.1. Synthesis of Powder

2.1.1. Preparation of CuO and ZnO Structures

The pristine CuO and ZnO powders were prepared using the polyol method by following two solutions.

- i. A total of 0.05 g of copper acetate (Cu(CH₃COO)₂, Sigma-Aldrich, Steinheim, Germany) was dissolved in 25 mL of ethylene glycol (C₂H₆O₂, Sigma-Aldrich) and stirred for 30 min at room temperature. Then, the resultant solution was heated at 150 °C for 40 min. After 20 min, the clear solution turned cloudy due to the formation of an organocopper precursor.
- ii. A total of 2 g of zinc acetate (Zn(CH₃COO)₂, Sigma-Aldrich) was added to 25 mL of ethylene glycol. Then, the mixture was stirred and heated at 150 °C for 6 h.

Both obtained powders were collected and washed by centrifugation with ethanol several times to remove side products. In this regard, the resultant particles were dried at

75 °C for 24 h, followed by annealing at 500 °C for 2 h, to obtain well-defined crystalline copper oxide and zinc oxide powders.

2.1.2. Synthesis of the CuO-ZnO Composite

First, the organocopper and zinc oxide precursors were prepared following the aforementioned steps without annealing. Then, two composite ratios with specific atomic ratios for Zn:Cu of 0.95:0.05 and 0.9:0.1, respectively, were synthesized at the same conditions. For the CuO-ZnO composite with a 0.9:0.1 ratio, 0.017 g of the obtained organocopper precursor was dissolved in 5 mL of isopropanol (C₃H₈O, Sigma Aldrich) and stirred at room temperature for 15 min. Afterward, 0.153 g of the above-mentioned prepared zinc oxide precursor was added to this mixture and stirred for 15 min to dissolve the ZnO precursor powder. The resultant solution was heated at 100 °C for 30 min. To obtain the precipitate, the solution was centrifuged three times with ethanol at 3500 rpm. The material was dried at 75 °C for 24 h and then calcinated at 500 °C for 2 h.

Two composite ratios have been synthesized to compare the gas sensing performance of the composite with bare CuO and ZnO powders. The specific atomic ratios for Zn:Cu of CuO-ZnO₉₅ and CuO-ZnO₉₀ are 0.95:0.05 and 0.9:0.1, respectively.

2.2. Characterization

The morphologies of samples were observed by high-resolution FESEM (MIRA3 FEG-SEM, TESCAN). Powder X-ray diffraction intensities were recorded with an X-ray diffractometer (Empyrean model, PANalytical, Almelo, The Netherlands) operating at 40 kV and 40 mA using a Cu-LFF ($\lambda = 1.54 \text{ \AA}$) source. The optical properties of materials were determined by a UV-vis spectrometer (UV-2600, Shimadzu, Kyoto, Japan).

2.3. Fabrication of the Sensor Device

For the gas sensing characterization, the nanostructures were fabricated on alumina substrates (Kyocera, Japan were 2 mm × 2 mm × 0.25 mm) using the drop-casting method. First, platinum (Pt) interdigitated electrical contacts and a Pt heater were deposited on top of the side and backside of the substrates using DC magnetron sputtering. Afterward, the prepared powders were dispersed in isopropyl alcohol and drop cast onto the alumina substrates using a Gilson dispenser (Figure S1a). Figure S1b depicts the gas sensing drop-cast material onto an Al₂O₃ substrate with Pt interdigitated deposition, providing insight into the distribution of the sensing material. Finally, the drop-cast materials underwent annealing at 450 °C to stabilize their electrical characteristics at high operating temperatures. Consequently, we selected 400 °C as the maximum temperature for conducting gas sensing studies.

Gas sensing measurements were conducted utilizing the flow-through technique within a thermostatic test chamber. In this method, a steady flow of synthetic air (0.3 L/min) was mixed with the desired concentration of gaseous species through a sealed chamber, which was kept at 20 °C, atmospheric pressure, and specific humidity level. More detailed information on the system can be found in previous sensor laboratory studies [30]. The humidity level was determined using a humidity sensor. To generate air saturated with water, synthetic dry air was initially passed through water maintained at a constant temperature and then through a condenser that was kept at the same temperature as the test chamber. The relative humidity was generated by mixing with dry air. To obtain the desired analyte concentrations, synthetic air was mixed with gas compounds from certified bottles. The sensing response of the fabricated structures towards reducing and oxidizing gases was calculated using the following equations, respectively:

$$\frac{(G_f - G_0)}{G_0} = \frac{\Delta G}{G_0} \quad (1)$$

$$\frac{(G_0 - G_f)}{G_f} = \frac{\Delta G}{G_f} \quad (2)$$

In Equations (1) and (2), G_0 represents the initial conductance of the n-type metal oxide sensor when exposed to air, while G_f denotes the stable conductance level of the sensor when the analyte compound is present.

3. Results and Discussion

3.1. Morphological Properties

Different morphological properties of CuO, ZnO, CuO-ZnO_95, and CuO-ZnO_90, characterized by FESEM, are shown in Figure 1a,b,e–i. The morphology of CuO powder is exhibited in Figure 1a,b. The low-magnification SEM image exhibits a microspheres hierarchical structure with a mean diameter size of 740 nm (Figure 1a,c). The high-magnification SEM images display that the CuO microspheres are composed of nanoparticles with an average particle size of 60 nm (Figure 1b,d). The morphology of the ZnO microstructure synthesized in the surfactant-free condition is shown in Figure 1e–g. The resultant zinc oxide precursor microstructure before the annealing process is displayed in Figure 1e. Figure 1f,g show the ZnO porous microstructure. Figure 1h exhibits that the porous microstructure of CuO-ZnO_95 is similar to the ZnO one, while the CuO-ZnO_90 structure presents CuO sphere-like and porous ZnO nanoparticles (Figure 1i).

The structure of the CuO is composed of nanometer-sized CuO crystals that are organized into larger, solid structures at the micrometer scale (microspheres) (Figure 1a,b). In the polyol process, the precipitates form a sphere shape due to minimize the surface energy. Over time, a particular process begins where these spherical particles start to dissolve a bit and then form new particles again. This process gradually changes their shape. Due to the relatively low concentration of the precursor, there are only a few nucleation centers. Furthermore, the growth of new particles on the surface of the spheres happens very slowly and is controlled by diffusion. In this regard, as this slow growth process continues, tiny particles attach themselves to the nucleation centers on the surface of the original spherical particles. Therefore, spheres shape changes and form particles on their surface [31–34]. The 3D hierarchical structure provides a high specific surface area and promotes the diffusion of analytes towards the surface. As can be seen in Figure 1f,g, the fabricated particles are porous structures after annealing treatment. EG molecules at high temperatures could produce OH^- ions, which reacted with Zn^{2+} to form $\text{Zn}(\text{OH})_2$ as the initial powder. Then, pores formed during the phase transition from $\text{Zn}(\text{OH})_2$ to ZnO at an annealing temperature of 500 °C, resulting in a high surface-to-volume ratio [35]. The ZnO porous structure is achieved without any additives, developing a low-cost, simple, and environmentally friendly method. To synthesize composite materials, both bare metal oxide precursors were prepared via the polyol method with the same conditions before calcination, and then CuO and ZnO were mixed by heating at 100 °C using isopropyl alcohol as a solvent. Hence, the morphological properties of composite structures were not significantly affected by the second step in their synthesis method due to the short reaction time.

3.2. Structural Properties

The crystal structures of CuO, ZnO, CuO-ZnO_95, and CuO-ZnO_90 were investigated by X-ray diffraction spectroscopy (XRD), as shown in Figure 2a. The synthesis of CuO includes a two-step process. First, copper acetate reacts with ethylene glycol (EG), producing organocopper precursors. Then, these organocopper precursors are annealed at 500 °C, leading to the formation of CuO powder. In this regard, the XRD pattern of the calcinated CuO sample confirms the formation of crystalline CuO after the heat treatment. The diffraction pattern of the CuO structure can be matched with monoclinic (space group: $C1\ 2/c\ 1$, space group number: 15, PDF No. 01-089-5897). No additional peak of any secondary Cu or Cu_2O phases is detected. Hence, the heat treatment step is essential for transforming the amorphous or precursor states into well-defined crystalline structures and preventing the formation of unwanted secondary phases.

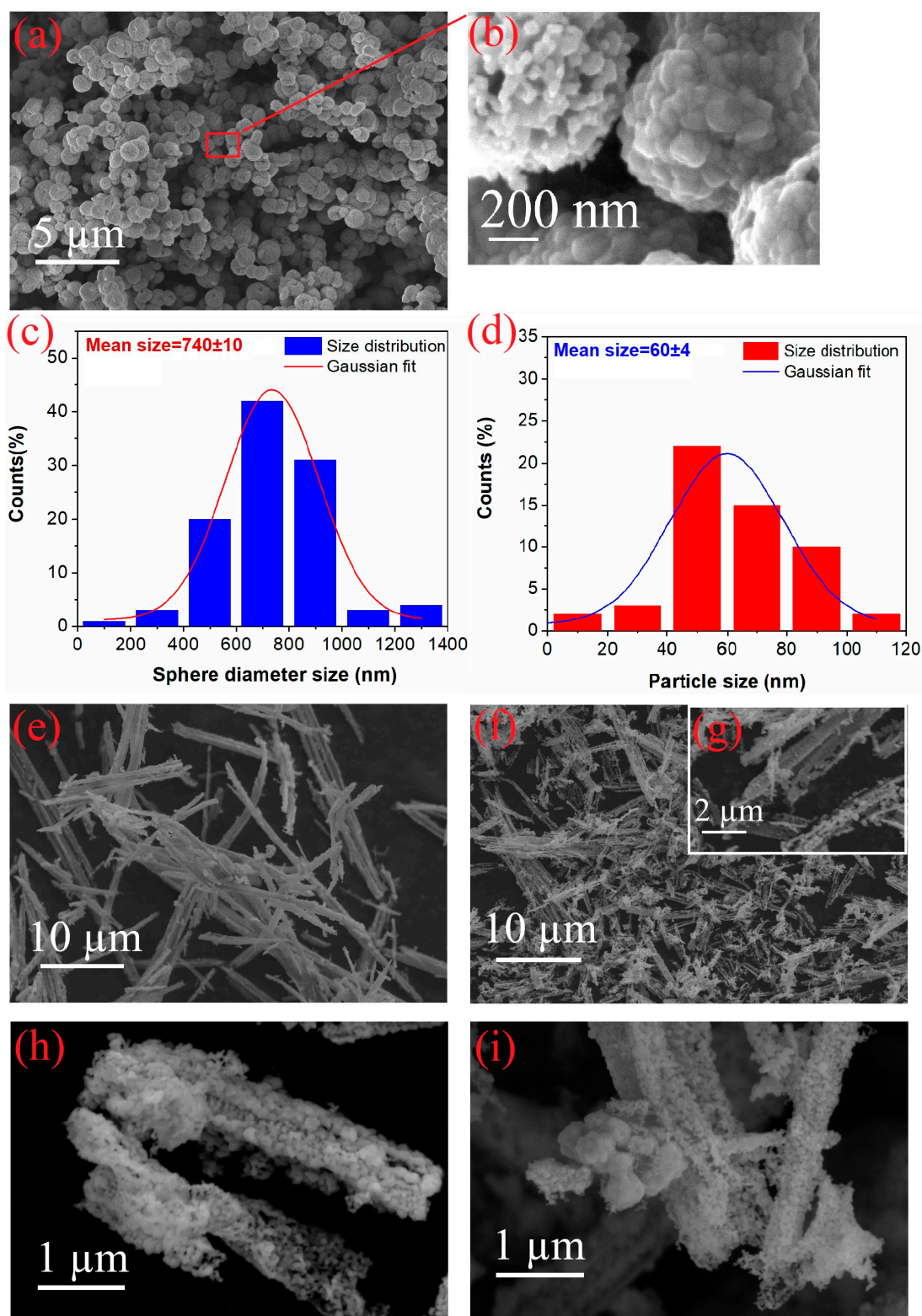


Figure 1. FESEM images of the prepared (a,b) CuO hierarchical structure synthesized using the polyol method; (c,d) size distribution histogram of the obtained CuO microsphere and nanoparticles; SEM images of the resultant (e) ZnO micro-rod using EG as a solvent before calcination; (f,g) the ZnO porous structure annealed at 500 $^{\circ}\text{C}$; synthesized composite utilizing isopropyl alcohol, where the proportions of Zn and Cu weight are (h) 0.95:0.05 (CuO-ZnO_95) and (i) 0.9:0.1 (CuO-ZnO_90).

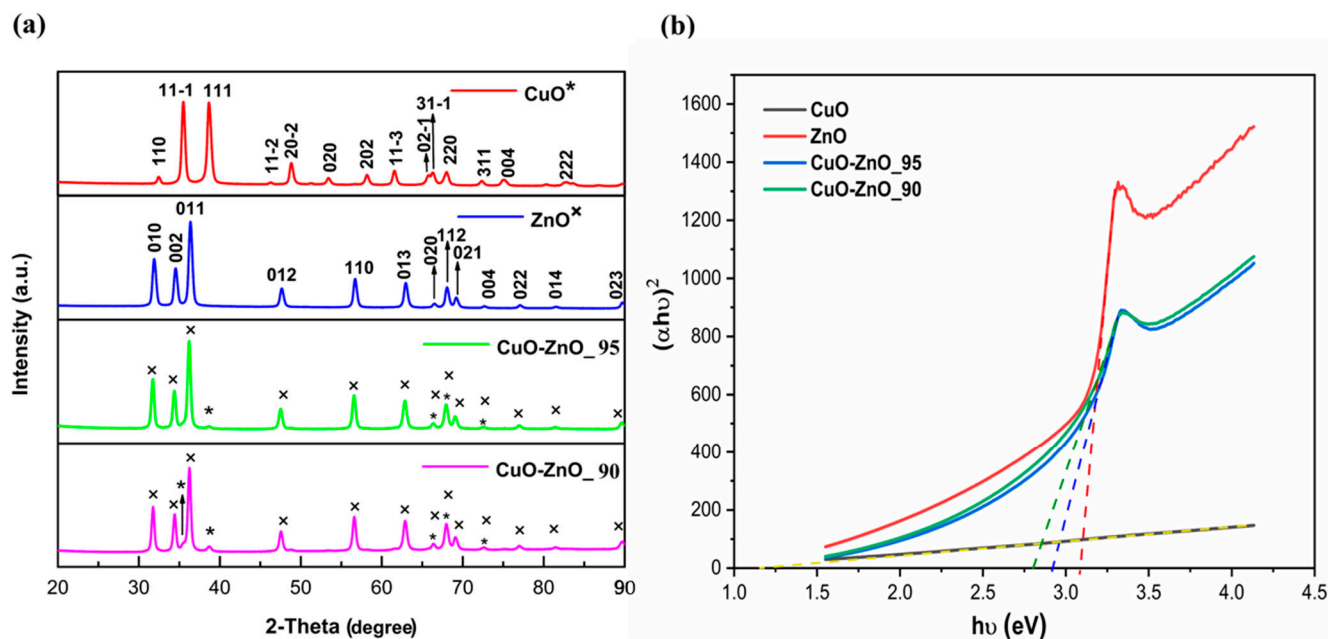


Figure 2. (a) XRD pattern of CuO, ZnO, CuO-ZnO₉₅, and CuO-ZnO₉₀ (“x” and “*” represent ZnO hexagonal crystalline peak and CuO monoclinic crystalline peak, respectively); (b) Tauc’s plot for band gap estimation of CuO, ZnO, CuO-ZnO₉₅, and CuO-ZnO₉₀.

The ZnO microstructure pattern reveals the crystalline structure of the hexagonal (space group: P 63 m c, space group number: 186, PDF No. 01-079-2205), and all diffraction peaks match well with the hexagonal without any secondary phases. The diffraction peaks of CuO-ZnO composites are almost the same as pure ZnO; however, few peaks correspond to the monoclinic CuO in the XRD pattern. When the organocopper precursor was added to the zinc acetate precursor solution (CuO-ZnO₉₅ and CuO-ZnO₉₀), one peak appeared at 38.73°, which corresponds to the (111) crystal plane of monoclinic CuO. In addition, peaks located at 66.3°, 68.03°, and 72.56° can be assigned to (31-1), (220), and (311) planes of monoclinic CuO and (020), (112), and (004) planes of hexagonal ZnO. Another extra peak at 35.46° was detected in the XRD pattern of CuO-ZnO₉₀, which can be assigned to the (11-1) plane of the CuO monoclinic. The diffraction peak intensity increases with an increasing organocopper precursor.

3.3. Optical Properties

The optical characteristics of the samples were evaluated through UV-vis spectroscopy to determine the band gap value of CuO, ZnO, CuO-ZnO₉₅, and CuO-ZnO₉₀. The band gap values were estimated by analyzing the absorption data (Figure S2 in Supplementary Material) using Equation (3), where A is a constant, α represents the absorption coefficient, and $h\nu$ corresponds to the energy of the incident photon. To find the band gap (E_g), a Tauc plot was created, plotting $(\alpha h\nu)^2$ against $h\nu$, and the E_g value was obtained by extending the linear section of the plot until α reached 0 (Figure 2b) [36]. The result exhibited a direct E_g of approximately 1.25 eV for CuO in agreement with the reported data (Table 1) [37]. Table 1 displays the obtained E_g of 3.09 eV for ZnO, which is different from the band gap range of 3.2–3.4 eV in the literature [38]. This small variation can be related to defects in the pure ZnO structure [39]. The calculated E_g for CuO-ZnO₉₅ and CuO-ZnO₉₀ were 2.92 and 2.81 eV. The band gap value is reduced with increasing the CuO concentration in the composite. The presence of Cu atoms in the ZnO lattice can create defects that affect the band structure and reduce the band gap energy value of the CuO-ZnO composite [40–42]. This increased carrier concentration leads to a reduction in the band gap, making it narrower [43]. On the other hand, when ZnO is mixed with CuO, it may provide more active sites at the surface of materials. These sites facilitate the transfer

of mass (molecules or atoms) and electrons between ZnO and CuO. As a result, there is a more efficient exchange of electrons between the two materials. This enhanced electron transfer is a key factor in reducing the band gap of the composite compared to the bare samples [43]. This lower band gap suggests that electron transfer processes are more likely to occur, which enhances gas sensing performance [44].

$$\alpha h\nu = A(h\nu - E_g)^{1/2} \quad (3)$$

Table 1. The band gap of ZnO, CuO, CuO-ZnO_95, and CuO-ZnO_90.

Samples	Band Gap (eV)
ZnO	3.09
CuO	1.25
CuO-ZnO_95	2.92
CuO-ZnO_90	2.81

3.4. Gas Sensing Performance

The operating temperature plays an important role in conductometric sensors due to its influence on the adsorption/desorption reaction on the gas sensing material surface. The gas sensing performances of the CuO microsphere, ZnO structure, CuO-ZnO_95, and CuO-ZnO_90 composites are investigated at temperatures ranging from 250 to 400 °C and 40% relative humidity. Figure 3 illustrates the gas sensing response of ZnO, CuO, CuO-ZnO_95, and CuO-ZnO_90 towards 5 ppm of NO₂ at different operating temperatures. The results indicate an enhancement in response of ZnO, CuO-ZnO_95, and CuO-ZnO_90 as the operating temperature increases up to 350 °C, followed by a reduction in values at 400 °C. Thus, the highest gas response of ZnO, CuO-ZnO_95, and CuO-ZnO_90 is observed at 350 °C, while the maximum response of the CuO nanostructure occurs at 250 °C. The gas sensing response shows enhancement with increasing temperature up to the optimal operating temperature. This improvement can be attributed to providing the higher activation energy necessary for NO₂ to initiate a reaction with the sensing material's surface. This process is facilitated by suitable adsorption surface energy and charge transfer. However, beyond the optimal temperature, the response value decreased, which could be related to the higher desorption rate of NO₂ compared to adsorption rates [45].

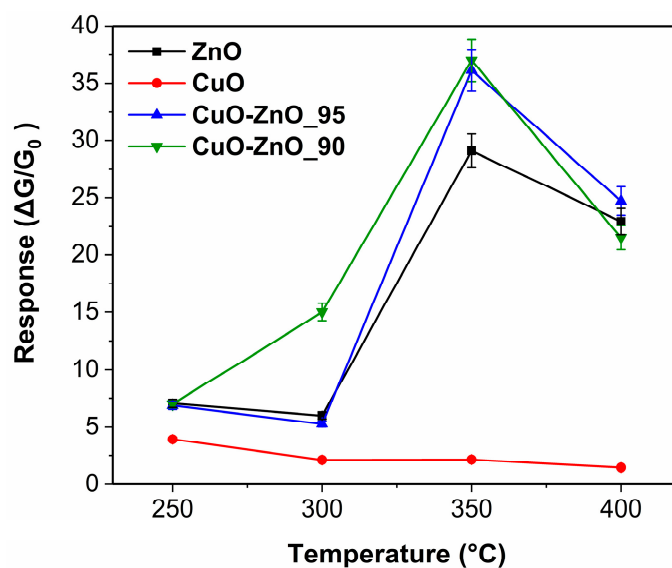


Figure 3. Gas sensing properties of pristine materials and their composite toward 5 ppm NO₂ at various temperatures.

Dynamic responses of the four samples demonstrate different behaviors (Figure 4a–d). The gas sensing measurements towards 1, 2, and 5 ppm NO₂ follow three steps: (1) exposing the surface of the material to air in the surrounding environment; (2) injecting NO₂ inside the chamber; and (3) purifying of the surface of the gas sensing material by restoring the airflow. As can be seen in Figure 4a, the conductance of ZnO, as expected by n-type metal oxide, decreases when exposed to NO₂ and returns to its baseline after restoring airflow. Furthermore, the CuO-ZnO₉₅ and CuO-ZnO₉₀ composite exhibits the same behaviors as the ZnO nanomaterial due to the presence of a high percentage of ZnO material (Figure 4c,d). On the other hand, increasing conductance of CuO confirms a p-type metal oxide behavior to NO₂ as an oxidizing gas (Figure 4b). As shown in Equations (4)–(7), oxygen molecules are adsorbed on the metal oxide surface and capture electrons from the conduction band, and then oxygen ions are formed on the surface of the material [46].

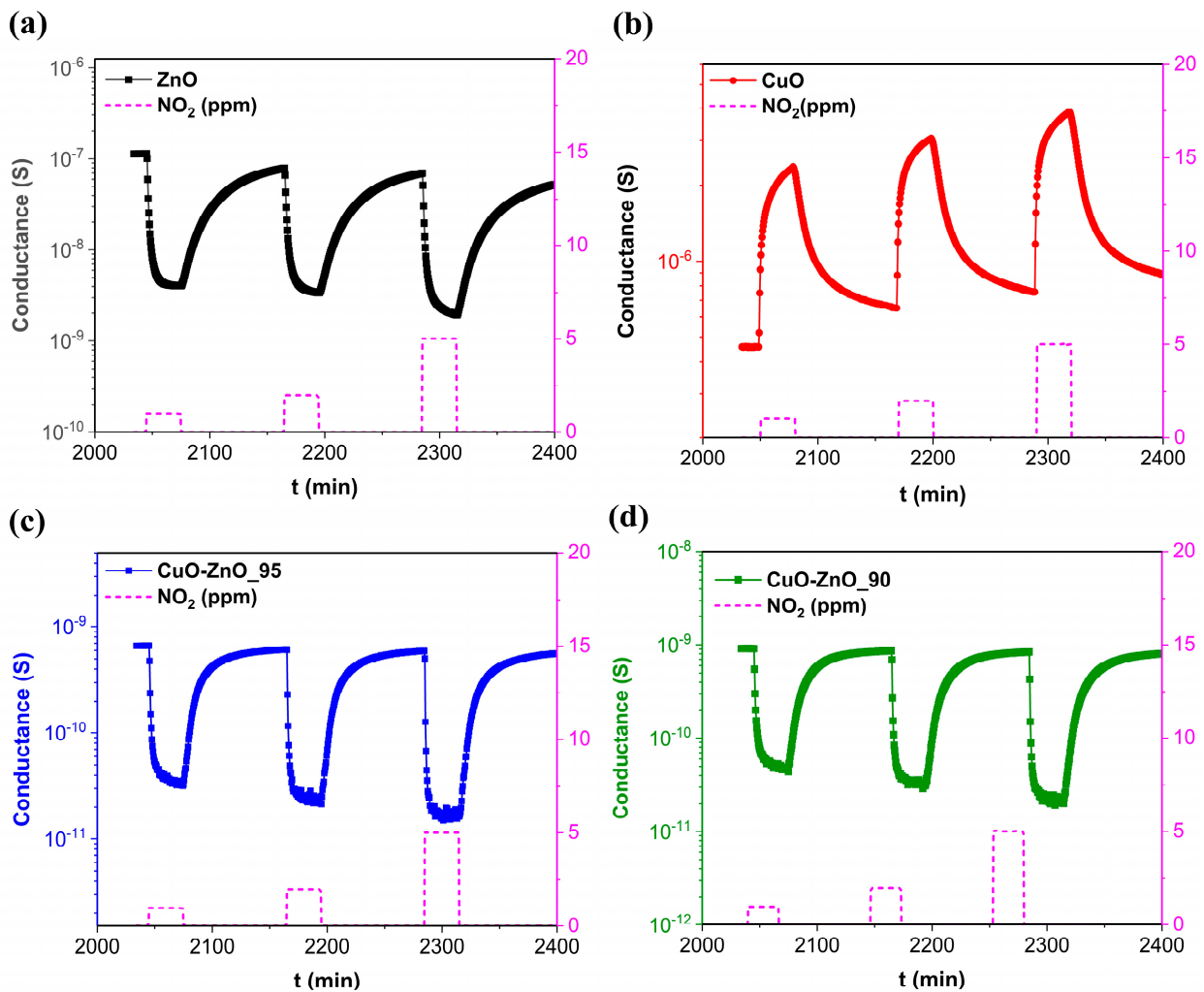
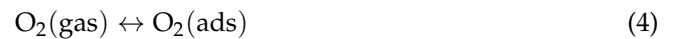


Figure 4. Dynamic response of (a) ZnO; (b) CuO; (c) CuO-ZnO₉₅; (d) CuO-ZnO₉₀ toward 1, 2, and 5 ppm NO₂ at their optimal operating temperature.

Upon exposure to NO₂ gas, the nanostructures undergo interactions with the NO₂ molecules adsorbed on the surface, leading to redox reactions, as outlined in Equation (8). The adsorbed NO₂ molecules can extract electrons from the materials' conduction band, leading to the production of species, as depicted in Equation (9) [47,48]. Additionally, due to the higher electronegativity of NO₂ molecules in comparison to oxygen, these adsorbed NO₂ molecules may react with oxygen species present on the surface (O²⁻ and O⁻), as illustrated in Equations (10) and (11) [47,49,50]. The sequence of these reaction processes is as follows:

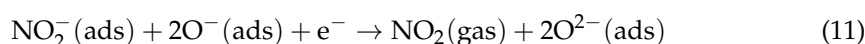
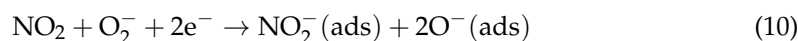
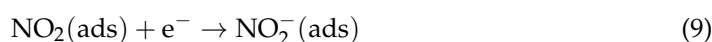


Figure 4a–d demonstrate a significant increase in composite resistance (10³ times) compared to pristine material owing to the band bending that can be related to the formation of the p-n junction at the surface of CuO and ZnO (formation of a Zn–O–Cu bond) [51–53]. In the p-n junction, electrons move from the n-type to the p-type metal oxide, while holes move from the p-type to n-type metal oxide until reaching an equilibrium state at the Fermi level [25,54]. Thus, the resistance increases due to the formation of a depletion layer. NO₂ mainly acts as an electron acceptor in surface reactions, resulting in an increase in the width of electron depletion layers and a decrease in the conductance of the sensors (n-type behavior) [50]. Furthermore, the dynamic response of CuO-ZnO₉₅ and CuO-ZnO₉₀ exhibit a stable baseline and rapid recovery compared to pristine materials. The addition of the CuO microsphere enhanced the response of the composite in comparison to bare materials (Figure 3), which may be attributed to the presence of more active sites, increasing the depletion layer and enabling charge transfer [55,56]. Additionally, the reduction in band gap energy implies a higher electron transfer and improved gas sensing performance [44].

Figure 5a illustrates gas sensing performances of CuO-ZnO₉₅ and CuO-ZnO₉₀ towards different concentrations (0.1, 0.2, 0.5, 1, 2, and 5 ppm) of NO₂ at 350 °C and a relative humidity of 40%. It can be observed that the gas sensing response of CuO-ZnO composites increased with the concentration of NO₂. Results (Table S1) demonstrate a good response to 100 ppb of NO₂ (response values of 1.6 and 1.2 for CuO-ZnO₉₅ and CuO-ZnO₉₀, respectively) and 200 ppb (response values of 3.3 and 2.8 for CuO-ZnO₉₅ and CuO-ZnO₉₀, respectively). The detection of low concentrations of NO₂ is significant for environmental monitoring. Also, the threshold limit value (TLV) of NO₂ (5 ppm) and the Scientific Committee on Occupational Exposure Limits (SCOEL) of the European Commission defines an 8 h time-weighted average (TWA) and a short-term exposure limit (STEL) (0.5 and 1 ppm, respectively) [57,58].

The humidity level can significantly influence the performance of gas sensors. In this regard, this study investigates the effect of humidity on CuO-ZnO₉₅ and CuO-ZnO₉₀ when exposed to 500 ppb of NO₂ at 350 °C (its optimum operating temperature). The behaviors of CuO-ZnO₉₅ and CuO-ZnO₉₀ sensors were examined at three relative humidity (RH) ranges: 0–40%, 40–80%, and 80–90%. Comparing the response of CuO-ZnO₉₅ and CuO-ZnO₉₀ sensors at various RH levels (as shown in Figure 5b), it is evident that humidity levels have a slight impact on the performance of sensors. Increasing RH from 0% (dry air) to 40% results in a 27% response increase in CuO-ZnO₉₅. In the case of CuO-ZnO₉₀, the response increase was 17%. Furthermore, the obtained results from 40% to 80% indicated an increase in the response of CuO-ZnO₉₅ and CuO-ZnO₉₀ by 7% and 13%, respectively. The response enhancement continues as RH is increased to 90%. Figure 5b demonstrates a 17% higher response of CuO-ZnO₉₅ when compared to 40% RH. Similarly, for CuO-ZnO₉₀, the response enhancement is even more significant at 90% RH, with an increase of 35%.

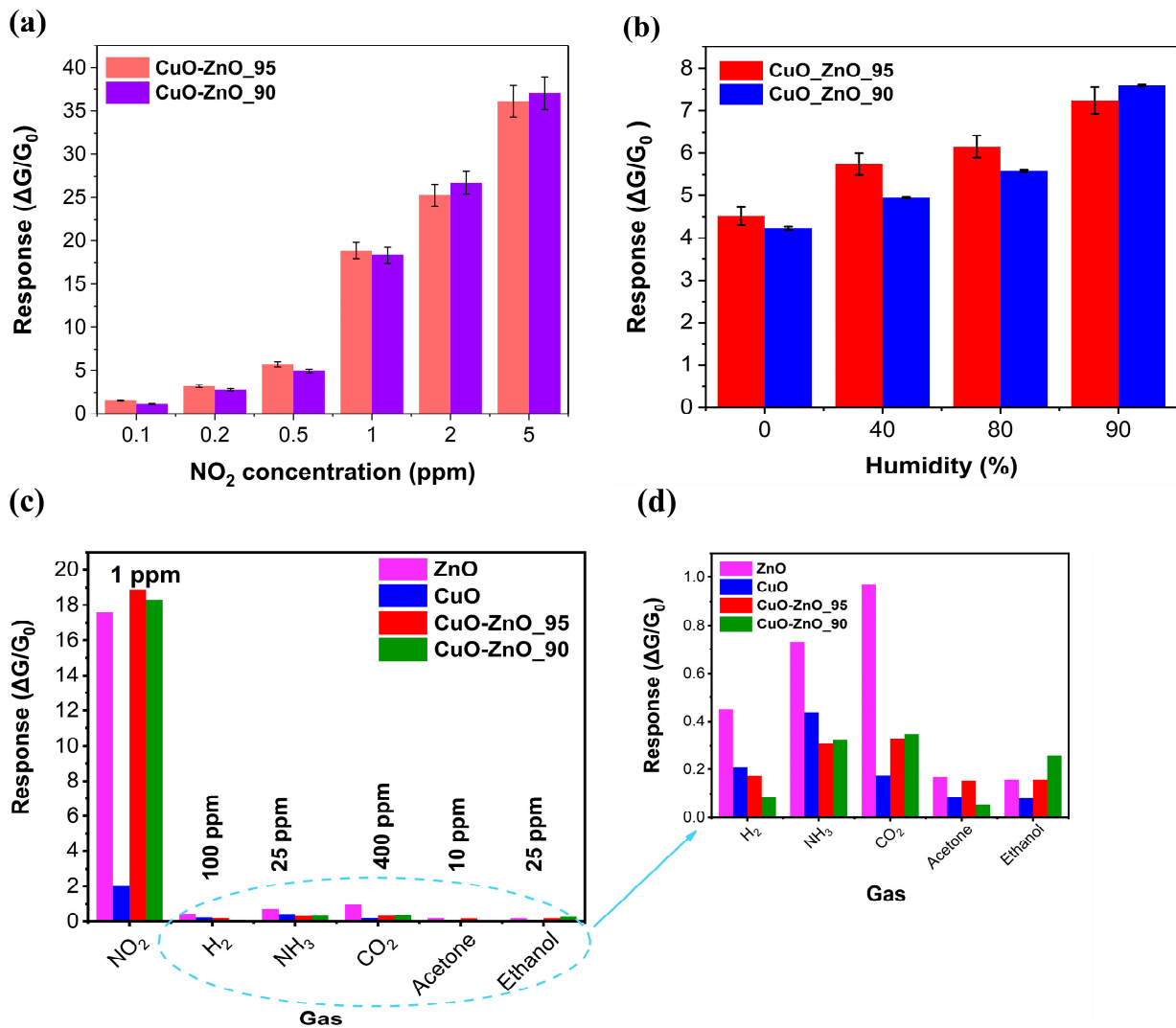


Figure 5. (a) Response of CuO-ZnO₉₅ and CuO-ZnO₉₀ towards various concentrations of NO₂ (0.1–5 ppm) at an operating temperature of 350 °C; (b) gas sensing response of CuO-ZnO₉₅ and CuO-ZnO₉₀ to 500 ppb of NO₂ at different relative humidity levels (0–90%) and an operating temperature of 350 °C; (c) response of ZnO, CuO, CuO-ZnO₉₅, and CuO-ZnO₉₀ towards various analytes (NO₂, H₂, NH₃, CO₂, acetone, and ethanol) at 350 °C (40% RH); (d) a magnified section in Figure (c) where the response of four samples towards interfering gases (H₂, NH₃, CO₂, acetone, and ethanol) can be clearly seen.

The effect of humidity on the electrical and sensing properties of gas sensors has been widely recognized, and this investigation extends the understanding of this phenomenon. Conductance behavior of composite materials at 350 °C reported in the Supplementary Material (Figure S3a); the conductance of the CuO-ZnO₉₅ and CuO-ZnO₉₀ was slightly higher at 40% RH compared to dry air conditions. Notably, at higher RH levels ranging from 40% to 90%, significant variations in conductance were not observed. The observed variations in response to changing humidity levels are attributed to the dissociation of water molecules on the sensor's surface, leading to the formation of hydroxyl (OH⁻) and proton (H⁺) groups [59,60]. These protons can contribute additional electrons to the sensing mechanism, thereby influencing the response towards NO₂. However, it is worth noting that the interaction of water molecules and other gaseous compounds with the surface of materials is a complex process and can be influenced by various factors, including operating conditions. Also, water may act as a catalyzer for the interaction between the analyte and the surface of the material [61,62]. Figure S3a displays good stability of electrical

conductance of both composites at 40–90% RH and a slight increase in conductance from 0 to 40% RH. At higher operating temperatures (350 °C), the influence of water molecules is decreased due to their evaporation.

Concerning selectivity, another crucial parameter of gas sensors, the responses of the four samples towards various gases were investigated (Figure 5c,d). As can be seen in Figure 5c, the response of four structures towards 100 ppm of H₂, 25 ppm of NH₃, 400 ppm of CO₂, 10 ppm of acetone, and 25 ppm of ethanol were analyzed at 350 °C. We utilized these different gas concentrations to simulate real-world scenarios and comprehensively evaluate how well the materials can distinguish between various gases in practical environments. Figure 5d exhibits higher responses of ZnO and CuO to hydrogen, ammonia, and carbon dioxide in comparison to the composite. Also, Figure S3b shows the response change in the sensor based on CuO-ZnO_90 at different operating temperatures. The sensors are selective to NO₂ at various operating temperatures (250–400 °C) (Figure S3b). Furthermore, the selectivity coefficient (K) of four sensors to NO₂ gas relative to other gases was evaluated to compare the composite selectivity with pristine materials. The selectivity coefficient (K) was determined using Equation (12) [63] as follows:

$$K = \frac{S_A}{S_B} \quad (12)$$

where S_A represents the sensor response to 5 ppm of NO₂ and S_B represents the sensor response to 100 ppm of H₂, 25 ppm of NH₃, 400 ppm of CO₂, 10 ppm of acetone, and 25 ppm of ethanol. A higher K value indicates a superior ability of the CuO-ZnO_95 and CuO-ZnO_90 sensors to differentiate NO₂ gas from other interfering gases (Figure S4). This confirms the enhanced selectivity of the composite sensors compared to sensors using bare materials for NO₂ gas. The excellent selectivity of four sensors towards NO₂ can be justified by three reasons. First, among various gases, NO₂ exhibits the lowest bond dissociation energy at 305.0 kJ/mol. In comparison, other gases have higher values: 436 kJ/mol for H₂, 391.0 kJ/mol for NH₃, 532 kJ/mol for CO₂, 798.9 kJ/mol for acetone, and 441.0 kJ/mol for ethanol (Table 2) [64–67]. This indicates that the dissociation of NO₂ molecules on the sensor's surface required less energy than other interfering gases, making the sensing reaction towards NO₂ highly favorable. Second, the higher response of four gas sensing materials towards NO₂ in comparison to reducing gases can be attributed to the electron affinity of NO₂ gas molecules (2.21 eV) [68], which is even higher than CO₂ as an oxidizing gas (0.6 eV) [69]. Finally, the superior selectivity of gas sensors towards NO₂ is also related to the acid-base properties of sensors. ZnO and CuO display strong basic and weak basic properties, respectively [57,70]. In general, active sites with acidic properties tend to facilitate the adsorption of reducing gases, which are predominantly basic in nature. Conversely, sites with basic properties promote the adsorption of acidic gases like NO₂ [57]. In this regard, in all sensing materials, the basic properties are dominant, resulting in an enhanced response to NO₂. Therefore, the high selectivity of the sensors is a result of the combination of the lower energy requirement for NO₂ dissociation, the high electron affinity of NO₂, and the acid-base properties of the sensor materials that favor the adsorption of acidic gases like NO₂. The excellent selectivity of NO₂ confirms its potential for practical application. Both composites reduce the interference from other gases at higher concentrations compared to NO₂, which is a desirable characteristic for a NO₂ sensor.

Table 3 presents the gas sensing performance of various materials to NO₂ at their optimum operating temperature. Comparison of the response of other materials is difficult due to different measurement conditions. However, these results confirm our excellent gas sensing performance towards NO₂ at 350 °C. Gas sensors with higher responses also towards lower concentrations of NO₂ compared with other works have been developed.

Table 2. Bond energy of tested gas molecules [64–67].

Gas	NO ₂	H ₂	NH ₃	CO ₂	Acetone	Ethanol
Bond	O–NO	H–H	H–NH ₂	O–CO	H–CH ₂ COCH ₃	H–OC ₂ H ₅
Bond energy (KJ/mole)	305.0	436.0	391.0	532.0	798.9	441.0

Table 3. Comparison of the gas sensing response of CuO- ZnO_90 towards NO₂ with the literature.

Sensing Materials	Operating Temperature (°C)	Concentration (ppm)	Response	Reference
CuO NPs	150	40	0.03 (R ₀ – R _f)/R _f	[22]
ZnO/g-C ₃ N ₄ nanocomposite	180	10	14.63 (R _f – R ₀)/R ₀	[71]
ZnO–CuO core–shell nanorods	300	10	0.5 (R ₀ – R _f)/R _f	[72]
ZnO nanowire/CuO nanoparticle	150	100	1.75 (R _f – R ₀)/R ₀	[55]
CuO-ZnO laminated heterostructure	350	29	9.2 (R ₀ /R _f)	[12]
CuO-ZnO nanocomposite	200	100	0.73 (R _f /R ₀)	[63]
hierarchical CuO-Co ₃ O ₄ spheres	160	20	0.48 (R _f – R ₀)/R ₀	[73]
MoS ₂ -ZnO nanowires	200	50	0.31 (R _f – R ₀)/R ₀	[74]
ZnO/rGO/Au hybrids	80	100	0.33 (R ₀ – R _f)/R _f	[75]
nanoporous CuO@ZnO	RT	5	3.37 (R ₀ – R _f)/R _f	[50]
CuO nanowires/ZnO NPs	250	100	4.1 (R ₀ /R _f)	[76]
Cu:ZnO thin film	200	100	3.26 (R _f – R ₀)/R ₀	[77]
ZnO nanorods	200	1	1.31 (I ₀ – I _f)/I _f	[78]
Ce-doped ZnO nanoarray	250	10	34.3 (R _f /R ₀)	[79]
Pt/ZnO/g-C ₃ N ₄	150	10	53 (R _f /R ₀)	[80]
CuO-ZnO_90	400	1	9.2 (G ₀ – G _f)/G _f	This work
CuO-ZnO_90	350	1	18.9 (G ₀ – G _f)/G _f	This work
CuO-ZnO_90	300	1	14.1 (G ₀ – G _f)/G _f	This work
CuO-ZnO_90	250	1	5.6 (G ₀ – G _f)/G _f	This work

Note: G₀: the initial conductance of the sensor in air; G_f: the stable conductance level of the sensor in gas; I₀: the current of the sensor in air; I_f: the current of the sensor in gas; R₀: resistance of the sensor in air; and R_f: resistance of the sensor in gas.

4. Conclusions

This study introduces an innovative approach that employs ethylene glycol as both a solvent and capping agent to effectively regulate the morphology and crystallization of bare metal oxides. The method is successful in producing hierarchical copper oxide (CuO) structures and porous zinc oxide (ZnO) through a straightforward and eco-friendly polyol process. CuO-ZnO composites were also synthesized, involving the dissolution of organocopper precursor in isopropanol, followed by mixing with prepared zinc oxide precursor and subsequent heating. SEM images showed the different morphological properties of CuO, ZnO, CuO-ZnO_95, and CuO-ZnO_90 samples. CuO microsphere hierarchical structures were observed, originating from the arrangement of nanometer-sized CuO crystals within micrometer-scale formations. The ZnO microstructure exhibited a porous rod-like morphology composed of nanoparticles, while CuO-ZnO_90 has CuO sphere-like components and porous ZnO particles. The structural investigations confirmed the formation of crystalline monoclinic CuO and hexagonal ZnO. The CuO-ZnO composites closely resembled pure ZnO in their diffraction patterns, with few peaks indicating the presence of monoclinic CuO. Band gaps of CuO and ZnO were calculated as 1.25 eV and 3.09 eV using Tauc's method. The presence of CuO in the composite reduced the band gap, which could be attributed to defects and increased carrier concentration caused by the incorporation of Cu atoms. This reduced band gap suggests enhanced gas sensing performance. Gas sensing measurements were conducted at various operating temperatures and humidity levels. The gas sensing responses of the materials towards NO₂ demonstrated a significant influence of both temperature and humidity, with CuO-ZnO composites displaying enhanced responses at higher humidity levels. Moreover, selectivity studies indicated excellent selectivity towards NO₂, exhibiting favorable responses compared to other interfering gases. The

high selectivity to NO₂ was attributed to the electron affinity, bond dissociation energy, and acid-base properties of the sensor materials. The CuO-ZnO composite exhibits excellent gas sensing performance, with improved sensitivity and selectivity compared to bare CuO and ZnO powders. The results highlight the potential of CuO-ZnO composites as materials for NO₂ gas sensing, contributing to the development of more efficient and reliable gas sensors for various industries and environmental monitoring.

Supplementary Materials: The following supporting information can be downloaded at: <https://www.mdpi.com/article/10.3390/chemosensors12040054/s1>, Figure S1: (a) Schematic representation of the fabrication of the gas sensor for electrical measurements and (b) SEM image of the gas sensing drop-cast material on Pt interdigitated and deposited on the Al₂O₃ substrate, Figure S2: UV-vis absorbance spectra, Figure S3: (a) Conductance of CuO-ZnO₉₅ and CuO-ZnO₉₀ at different relative humidities (0–90%) and (b) response of CuO-ZnO₉₀ towards 1 ppm of NO₂, 100 ppm of H₂, 25 ppm of NH₃, 400 ppm of CO₂, 10 ppm of acetone, and 25 ppm of ethanol, Figure S4: Selectivity coefficient of ZnO, CuO, CuO-ZnO₉₅, and CuO-ZnO₉₀ to 5 ppm of NO₂; Table S1: Response of CuO-ZnO₉₅ and CuO-ZnO₉₀ towards various concentrations of NO₂ at 350 °C.

Author Contributions: Conceptualization, H.P., M.P., M.B. and E.C.; methodology, H.P. and E.C.; validation, E.C.; formal analysis, H.P., M.P. and M.B.; investigation, H.P. and E.C.; resources, E.C.; data curation, H.P.; writing—original draft preparation, H.P.; writing—review and editing, E.C., M.P. and M.B.; visualization, H.P. and E.C.; supervision, E.C.; project administration, E.C.; funding acquisition, E.C. All authors have read and agreed to the published version of the manuscript.

Funding: This study was carried out within the MOST “Sustainable Mobility National Research Center” and received funding from the European Union Next-Generation EU (“PIANO NAZIONALE DI RIPRESA E RESILIENZA (PNRR)–MISSIONE 4 COMPONENTE 2, INVESTIMENTO 1.4—D.D. 1033 17/06/2022, CN00000023”) and the Spoke 5 “Light Vehicle and Active Mobility”. This manuscript reflects only the authors’ views and opinions; neither the European Union nor the European Commission can be considered responsible for them.

Institutional Review Board Statement: Not applicable.

Informed Consent Statement: Not applicable.

Data Availability Statement: Data are contained within the article.

Conflicts of Interest: The authors declare no conflicts of interest.

References

1. Faiz, A. Automotive emissions in developing countries-relative implications for global warming, acidification and urban air quality. *Transp. Res. Part A Policy Pract.* **1993**, *27*, 167–186. [[CrossRef](#)]
2. Le, D.T.T.; Long, N.D.H.; Xuan, C.T.; Van Toan, N.; Hung, C.M.; Van Duy, N.; Theu, L.T.; Dinh, V.A.; Hoa, N.D. Porous CoFe₂O₄ nanorods: VOC gas-sensing characteristics and DFT calculation. *Sens. Actuators B Chem.* **2023**, *379*, 133286.
3. Deng, S.; Liu, X.; Chen, N.; Deng, D.; Xiao, X.; Wang, Y. A highly sensitive VOC gas sensor using p-type mesoporous Co₃O₄ nanosheets prepared by a facile chemical coprecipitation method. *Sens. Actuators B Chem.* **2016**, *233*, 615–623. [[CrossRef](#)]
4. Zyryanov, G.V.; Kang, Y.; Rudkevich, D.M. Sensing and Fixation of NO₂/N₂O₄ by Calix[4]Arenes. *J. Am. Chem. Soc.* **2003**, *125*, 2997–3007. [[CrossRef](#)] [[PubMed](#)]
5. Tamvakos, A.; Korir, K.; Tamvakos, D.; Calestani, D.; Cicero, G.; Pullini, D. NO₂ gas sensing mechanism of ZnO thin-film transducers: Physical experiment and theoretical correlation study. *ACS Sens.* **2016**, *1*, 406–412. [[CrossRef](#)]
6. Frampton, M.W.; Boscia, J.; Roberts, N.J., Jr.; Azadniv, M.; Torres, A.; Cox, C.; Morrow, P.E.; Nichols, J.; Chalupa, D.; Frasier, L.M. Nitrogen dioxide exposure: Effects on airway and blood cells. *Am. J. Physiol. Lung Cell. Mol. Physiol.* **2002**, *282*, L155–L165. [[CrossRef](#)] [[PubMed](#)]
7. Weinmayr, G.; Romeo, E.; De Sario, M.; Weiland, S.K.; Forastiere, F. Short-term effects of PM10 and NO₂ on respiratory health among children with asthma or asthma-like symptoms: A systematic review and meta-analysis. *Environ. Health Perspect.* **2010**, *118*, 449–457. [[CrossRef](#)] [[PubMed](#)]
8. Greenberg, N.; Carel, R.S.; Derazne, E.; Bibi, H.; Shpriz, M.; Tzur, D.; Portnov, B.A. Different effects of long-term exposures to SO₂ and NO₂ air pollutants on asthma severity in young adults. *J. Toxicol. Environ. Health Part A* **2016**, *79*, 342–351. [[CrossRef](#)] [[PubMed](#)]
9. Gillespie-Bennett, J.; Pierse, N.; Wickens, K.; Crane, J.; Howden-Chapman, P. The respiratory health effects of nitrogen dioxide in children with asthma. *Eur. Respir. J.* **2011**, *38*, 303–309. [[CrossRef](#)] [[PubMed](#)]

10. Andersen, Z.J.; Bønnelykke, K.; Hvidberg, M.; Jensen, S.S.; Ketzel, M.; Loft, S.; Sørensen, M.; Tjønneland, A.; Overvad, K.; Raaschou-Nielsen, O. Long-term exposure to air pollution and asthma hospitalisations in older adults: A cohort study. *Thorax* **2012**, *67*, 6–11. [[CrossRef](#)] [[PubMed](#)]
11. Mele, M.; Magazzino, C.; Schneider, N.; Strezov, V. NO₂ levels as a contributing factor to COVID-19 deaths: The first empirical estimate of threshold values. *Environ. Res.* **2021**, *194*, 110663. [[CrossRef](#)] [[PubMed](#)]
12. Yang, L.; Xie, C.; Zhang, G.; Zhao, J.; Yu, X.; Zeng, D.; Zhang, S. Enhanced response to NO₂ with CuO/ZnO laminated heterostructured configuration. *Sens. Actuators B Chem.* **2014**, *195*, 500–508. [[CrossRef](#)]
13. Fischer, S.; Pohle, R.; Farber, B.; Proch, R.; Kaniuk, J.; Fleischer, M.; Moos, R. Method for detection of NO_x in exhaust gases by pulsed discharge measurements using standard zirconia-based lambda sensors. *Sens. Actuators B Chem.* **2010**, *147*, 780–785. [[CrossRef](#)]
14. Geupel, A.; Schönauer, D.; Röder-Roith, U.; Kubinski, D.J.; Mulla, S.; Ballinger, T.H.; Chen, H.-Y.; Visser, J.H.; Moos, R. Integrating nitrogen oxide sensor: A novel concept for measuring low concentrations in the exhaust gas. *Sens. Actuators B Chem.* **2010**, *145*, 756–761. [[CrossRef](#)]
15. Dey, A. Semiconductor metal oxide gas sensors: A review. *Mater. Sci. Eng. B* **2018**, *229*, 206–217. [[CrossRef](#)]
16. Fierro, J.L.G. *Metal Oxides: Chemistry and Applications*; CRC Press: Boca Raton, FL, USA, 2005.
17. Kumbhakar, P.; Gowda, C.C.; Mahapatra, P.L.; Mukherjee, M.; Malviya, K.D.; Chaker, M.; Chandra, A.; Lahiri, B.; Ajayan, P.; Jariwala, D. Emerging 2D metal oxides and their applications. *Mater. Today* **2021**, *45*, 142–168. [[CrossRef](#)]
18. Li, Z.; Li, H.; Wu, Z.; Wang, M.; Luo, J.; Torun, H.; Hu, P.; Yang, C.; Grundmann, M.; Liu, X. Advances in designs and mechanisms of semiconducting metal oxide nanostructures for high-precision gas sensors operated at room temperature. *Mater. Horiz.* **2019**, *6*, 470–506. [[CrossRef](#)]
19. Korotcenkov, G.; Cho, B. Metal oxide composites in conductometric gas sensors: Achievements and challenges. *Sens. Actuators B Chem.* **2017**, *244*, 182–210. [[CrossRef](#)]
20. Zhang, Q.; Zhang, K.; Xu, D.; Yang, G.; Huang, H.; Nie, F.; Liu, C.; Yang, S. CuO nanostructures: Synthesis, characterization, growth mechanisms, fundamental properties, and applications. *Prog. Mater. Sci.* **2014**, *60*, 208–337. [[CrossRef](#)]
21. Chen, X.; Zhao, S.; Zhou, P.; Cui, B.; Liu, W.; Wei, D.; Shen, Y. Room-temperature NO₂ sensing properties and mechanism of CuO nanorods with Au functionalization. *Sens. Actuators B Chem.* **2021**, *328*, 129070. [[CrossRef](#)]
22. Das, A.; Venkataramana, B.; Partheephan, D.; Prasad, A.; Dhara, S.; Tyagi, A. Facile synthesis of nanostructured CuO for low temperature NO₂ sensing. *Phys. E Low-Dimens. Syst. Nanostruct.* **2013**, *54*, 40–44. [[CrossRef](#)]
23. Navale, Y.; Navale, S.; Galluzzi, M.; Stadler, F.; Debnath, A.; Ramgir, N.; Gadkari, S.; Gupta, S.; Aswal, D.; Patil, V. Rapid synthesis strategy of CuO nanocubes for sensitive and selective detection of NO₂. *J. Alloys Compd.* **2017**, *708*, 456–463. [[CrossRef](#)]
24. Li, Q.; Zeng, W.; Li, Y. Metal oxide gas sensors for detecting NO₂ in industrial exhaust gas: Recent developments. *Sens. Actuators B Chem.* **2022**, *359*, 131579. [[CrossRef](#)]
25. Huang, J.; Dai, Y.; Gu, C.; Sun, Y.; Liu, J. Preparation of porous flower-like CuO/ZnO nanostructures and analysis of their gas-sensing property. *J. Alloys Compd.* **2013**, *575*, 115–122. [[CrossRef](#)]
26. Sankaran, A.; Kumaraguru, K. The novel two step synthesis of CuO/ZnO and CuO/CdO nanocatalysts for enhancement of catalytic activity. *J. Mol. Struct.* **2020**, *1221*, 128772. [[CrossRef](#)]
27. Figlarz, M.; Fievet, F.; Lagier, J.-P. Process for the Reduction of Metallic Compounds by Polyols, and Metallic Powders Obtained by This Process. U.S. Patent 4539041, 3 September 1985.
28. Sun, Y.; Xia, Y. Large-scale synthesis of uniform silver nanowires through a soft, self-seeding, polyol process. *Adv. Mater.* **2002**, *14*, 833–837. [[CrossRef](#)]
29. Dong, H.; Chen, Y.-C.; Feldmann, C. Polyol synthesis of nanoparticles: Status and options regarding metals, oxides, chalcogenides, and non-metal elements. *Green Chem.* **2015**, *17*, 4107–4132. [[CrossRef](#)]
30. Barreca, D.; Gasparotto, A.; Maccato, C.; Maragno, C.; Tondello, E.; Comini, E.; Sberveglieri, G. Columnar CeO₂ nanostructures for sensor application. *Nanotechnology* **2007**, *18*, 125502. [[CrossRef](#)]
31. Cao, A.-M.; Hu, J.-S.; Liang, H.-P.; Song, W.-G.; Wan, L.-J.; He, X.-L.; Gao, X.-G.; Xia, S.-H. Hierarchically structured cobalt oxide (Co₃O₄): The morphology control and its potential in sensors. *J. Phys. Chem. B* **2006**, *110*, 15858–15863. [[CrossRef](#)] [[PubMed](#)]
32. Liu, J.; Huang, X.; Li, Y.; Sulieman, K.; He, X.; Sun, F. Hierarchical nanostructures of cupric oxide on a copper substrate: Controllable morphology and wettability. *J. Mater. Chem.* **2006**, *16*, 4427–4434. [[CrossRef](#)]
33. Suber, L.; Sondi, I.; Matijević, E.; Goia, D.V. Preparation and the mechanisms of formation of silver particles of different morphologies in homogeneous solutions. *J. Colloid Interface Sci.* **2005**, *288*, 489–495. [[CrossRef](#)]
34. Cao, A.-M.; Monnell, J.D.; Matranga, C.; Wu, J.-M.; Cao, L.-L.; Gao, D. Hierarchical nanostructured copper oxide and its application in arsenic removal. *J. Phys. Chem. C* **2007**, *111*, 18624–18628. [[CrossRef](#)]
35. Ghoshal, T.; Kar, S.; Chaudhuri, S. ZnO doughnuts: Controlled synthesis, growth mechanism, and optical properties. *Cryst. Growth Des.* **2007**, *7*, 136–141. [[CrossRef](#)]
36. Makuła, P.; Pacia, M.; Macyk, W. How to correctly determine the band gap energy of modified semiconductor photocatalysts based on UV–Vis spectra. *J. Phys. Chem. Lett.* **2018**, *9*, 6814–6817. [[CrossRef](#)] [[PubMed](#)]
37. Mashock, M.; Yu, K.; Cui, S.; Mao, S.; Lu, G.; Chen, J. Modulating gas sensing properties of CuO nanowires through creation of discrete nanosized p–n junctions on their surfaces. *ACS Appl. Mater. Interfaces* **2012**, *4*, 4192–4199. [[CrossRef](#)]

38. Marotti, R.; Giorgi, P.; Machado, G.; Dalchiele, E. Crystallite size dependence of band gap energy for electrodeposited ZnO grown at different temperatures. *Sol. Energy Mater. Sol. Cells* **2006**, *90*, 2356–2361. [[CrossRef](#)]
39. Shan, F.; Yu, Y. Band gap energy of pure and Al-doped ZnO thin films. *J. Eur. Ceram. Soc.* **2004**, *24*, 1869–1872. [[CrossRef](#)]
40. Datta, N.; Ramgir, N.S.; Kumar, S.; Veerender, P.; Kaur, M.; Kailasaganapathi, S.; Debnath, A.; Aswal, D.; Gupta, S. Role of various interfaces of CuO/ZnO random nanowire networks in H₂S sensing: An impedance and Kelvin probe analysis. *Sens. Actuators B Chem.* **2014**, *202*, 1270–1280. [[CrossRef](#)]
41. Morales-Mendoza, J.E.; Herrera-Pérez, G.; Fuentes-Cobas, L.; Hermida-Montero, L.A.; Pariona, N.; Paraguay-Delgado, F. Synthesis, structural and optical properties of Cu doped ZnO and CuO–ZnO composite nanoparticles. *Nano-Struct. Nano-Objects* **2023**, *34*, 100967. [[CrossRef](#)]
42. Harish, S.; Archana, J.; Sabarinathan, M.; Navaneethan, M.; Nisha, K.D.; Ponnusamy, S.; Muthamizhchelvan, C.; Ikeda, H.; Aswal, D.K.; Hayakawa, Y. Controlled structural and compositional characteristic of visible light active ZnO/CuO photocatalyst for the degradation of organic pollutant. *Appl. Surf. Sci.* **2017**, *418*, 103–112. [[CrossRef](#)]
43. Musa, A.M.M.; Rasadujaman, M.; Gafur, M.A.; Jamil, A.T.M.K. Synthesis and characterization of dip-coated ZnO–CuO composite thin film for room-temperature CO₂ gas sensing. *Thin Solid Film.* **2023**, *773*, 139838. [[CrossRef](#)]
44. Krishna, K.G.; Parne, S.R.; Nagaraju, P. An optical study of heterojunction n-ZnO/p-CuO nanosheets and detection of n-butanol vapour at room temperature. *J. Mater. Sci.* **2023**, *58*, 15660–15675. [[CrossRef](#)]
45. Aqeel, T.; Galstyan, V.; Comini, E.; Bumajdad, A. Efficient one-pot synthesis of antimony-containing mesoporous tin dioxide nanostructures for gas-sensing applications. *Arab. J. Chem.* **2023**, *16*, 104797. [[CrossRef](#)]
46. Madou, M.J.; Morrison, S.R. *Chemical Sensing with Solid State Devices*; Elsevier: Amsterdam, The Netherlands, 2012.
47. Bai, H.; Guo, H.; Wang, J.; Dong, Y.; Liu, B.; Xie, Z.; Guo, F.; Chen, D.; Zhang, R.; Zheng, Y. A room-temperature NO₂ gas sensor based on CuO nanoflakes modified with rGO nanosheets. *Sens. Actuators B Chem.* **2021**, *337*, 129783. [[CrossRef](#)]
48. Zhong, Y.; Li, W.; Zhao, X.; Jiang, X.; Lin, S.; Zhen, Z.; Chen, W.; Xie, D.; Zhu, H. High-response room-temperature NO₂ sensor and ultrafast humidity sensor based on SnO₂ with rich oxygen vacancy. *ACS Appl. Mater. Interfaces* **2019**, *11*, 13441–13449. [[CrossRef](#)] [[PubMed](#)]
49. Patil, V.; Kumbhar, S.; Vanalakar, S.; Tarwal, N.; Mali, S.; Kim, J.; Patil, P. Gas sensing properties of 3D mesoporous nanostructured ZnO thin films. *New J. Chem.* **2018**, *42*, 13573–13580. [[CrossRef](#)]
50. Govind, A.; Bharathi, P.; Mohan, M.K.; Archana, J.; Harish, S.; Navaneethan, M. Highly sensitive near room temperature operable NO₂ gas-sensor for enhanced selectivity via nanoporous CuO@ZnO heterostructures. *J. Environ. Chem. Eng.* **2023**, *11*, 110056. [[CrossRef](#)]
51. Wang, X.; Li, S.; Xie, L.; Li, X.; Lin, D.; Zhu, Z. Low-temperature and highly sensitivity H₂S gas sensor based on ZnO/CuO composite derived from bimetal metal-organic frameworks. *Ceram. Int.* **2020**, *46*, 15858–15866. [[CrossRef](#)]
52. Chen, Y.; Shen, Z.; Jia, Q.; Zhao, J.; Zhao, Z.; Ji, H. A CuO–ZnO nanostructured p–n junction sensor for enhanced N-butanol detection. *RSC Adv.* **2016**, *6*, 2504–2511. [[CrossRef](#)]
53. Zhao, S.; Shen, Y.; Hao, F.; Kang, C.; Cui, B.; Wei, D.; Meng, F. Pn junctions based on CuO-decorated ZnO nanowires for ethanol sensing application. *Appl. Surf. Sci.* **2021**, *538*, 148140. [[CrossRef](#)]
54. Zhang, Y.-B.; Yin, J.; Li, L.; Zhang, L.-X.; Bie, L.-J. Enhanced ethanol gas-sensing properties of flower-like p-CuO/n-ZnO heterojunction nanorods. *Sens. Actuators B Chem.* **2014**, *202*, 500–507. [[CrossRef](#)]
55. Navale, Y.H.; Navale, S.T.; Stadler, F.J.; Ramgir, N.S.; Patil, V.B. Enhanced NO₂ sensing aptness of ZnO nanowire/CuO nanoparticle heterostructure-based gas sensors. *Ceram. Int.* **2019**, *45*, 1513–1522. [[CrossRef](#)]
56. Miller, D.R.; Akbar, S.A.; Morris, P.A. Nanoscale metal oxide-based heterojunctions for gas sensing: A review. *Sens. Actuators B Chem.* **2014**, *204*, 250–272. [[CrossRef](#)]
57. Kwon, Y.J.; Kang, S.Y.; Mirzaei, A.; Choi, M.S.; Bang, J.H.; Kim, S.S.; Kim, H.W. Enhancement of gas sensing properties by the functionalization of ZnO-branched SnO₂ nanowires with Cr₂O₃ nanoparticles. *Sens. Actuators B Chem.* **2017**, *249*, 656–666. [[CrossRef](#)]
58. Matatagui, D.; Lopez-Sanchez, J.; Pena, A.; Serrano, A.; Del Campo, A.; de la Fuente, O.R.; Carmona, N.; Navarro, E.; Marin, P.; del Carmen Horrillo, M. Ultrasensitive NO₂ gas sensor with insignificant NH₃-interference based on a few-layered mesoporous graphene. *Sens. Actuators B Chem.* **2021**, *335*, 129657. [[CrossRef](#)]
59. Galstyan, V.; Poli, N.; D’Arco, A.; Macis, S.; Lupi, S.; Comini, E. A novel approach for green synthesis of WO₃ nanomaterials and their highly selective chemical sensing properties. *J. Mater. Chem. A* **2020**, *8*, 20373–20385. [[CrossRef](#)]
60. Agmon, N. The grotthuss mechanism. *Chem. Phys. Lett.* **1995**, *244*, 456–462. [[CrossRef](#)]
61. Pakdel, H.; Galstyan, V.; D’Arco, A.; Mancini, T.; Lupi, S.; Moumen, A.; Borsi, M.; Comini, E. Synthesis of WO₃ nanopowder using a green surfactant for efficient gas sensing applications. *Ceram. Int.* **2023**, *49*, 30501–30509. [[CrossRef](#)]
62. Boyle, J.; Jones, K. The effects of CO, water vapor and surface temperature on the conductivity of a SnO₂ gas sensor. *J. Electron. Mater.* **1977**, *6*, 717–733. [[CrossRef](#)]
63. Mali, S.M.; Narwade, S.S.; Navale, Y.H.; Tayade, S.B.; Diggraskar, R.V.; Patil, V.B.; Kumbhar, A.S.; Sathe, B.R. Heterostructural CuO–ZnO Nanocomposites: A Highly Selective Chemical and Electrochemical NO₂ Sensor. *ACS Omega* **2019**, *4*, 20129–20141. [[CrossRef](#)] [[PubMed](#)]
64. Bang, J.H.; Choi, M.S.; Mirzaei, A.; Kwon, Y.J.; Kim, S.S.; Kim, T.W.; Kim, H.W. Selective NO₂ sensor based on Bi₂O₃ branched SnO₂ nanowires. *Sens. Actuators B Chem.* **2018**, *274*, 356–369. [[CrossRef](#)]

65. Shi, J.; Cheng, Z.; Gao, L.; Zhang, Y.; Xu, J.; Zhao, H. Facile synthesis of reduced graphene oxide/hexagonal WO₃ nanosheets composites with enhanced H₂S sensing properties. *Sens. Actuators B Chem.* **2016**, *230*, 736–745. [[CrossRef](#)]
66. Zhang, D. *Morphology Genetic Materials Templated from Nature Species*; Springer Science & Business Media: Berlin/Heidelberg, Germany, 2014.
67. Karthik, T.; Martínez-García, H.; Ortiz-Chi, F.; Espinosa-González, C.; Torres-Torres, J.; Hernandez, A.; Godavarthi, S.; Kesarla, M. CO₂ gas sensing properties of graphitic carbon nitride (g-C₃N₄) thin films. *Diam. Relat. Mater.* **2023**, *133*, 109736. [[CrossRef](#)]
68. Liu, Z.; Yu, L.; Guo, F.; Liu, S.; Qi, L.; Shan, M.; Fan, X. Facial development of high performance room temperature NO₂ gas sensors based on ZnO nanowalls decorated rGO nanosheets. *Appl. Surf. Sci.* **2017**, *423*, 721–727. [[CrossRef](#)]
69. Compton, R.; Reinhardt, P.; Cooper, C. Collisional ionization of Na, K, and Cs by CO₂, COS, and CS₂: Molecular electron affinities. *J. Chem. Phys.* **1975**, *63*, 3821–3827. [[CrossRef](#)]
70. Abreu, N.J.; Valdés, H.; Zaror, C.A.; de Oliveira, T.F.; Azzolina-Jury, F.; Thibault-Starzyk, F. Evidence of Synergy Effects between Zinc and Copper Oxides with Acidic Sites on Natural Zeolite during Photocatalytic Oxidation of Ethylene Using Operando DRIFTS Studies. *Catalysts* **2023**, *13*, 610. [[CrossRef](#)]
71. Simon Patrick, D.; Govind, A.; Bharathi, P.; Krishna Mohan, M.; Harish, S.; Archana, J.; Navaneethan, M. Hierarchical ZnO/g-C₃N₄ nanocomposites for enhanced NO₂ gas sensing applications. *Appl. Surf. Sci.* **2023**, *609*, 155337. [[CrossRef](#)]
72. Jin, C.; Kim, H.; Park, S.; Choi, S.W.; Kim, S.S.; Lee, C. NO₂ gas sensing properties of ZnO sheathed CuO nanorods. *Surf. Interface Anal.* **2012**, *44*, 1534–1537. [[CrossRef](#)]
73. Fang, H.; Li, S.; Zhao, H.; Deng, J.; Wang, D.; Li, J. Enhanced NO₂ gas sensing performance by hierarchical CuO–Co₃O₄ spheres. *Sens. Actuators B Chem.* **2022**, *352*, 131068. [[CrossRef](#)]
74. Zhao, S.; Wang, G.; Liao, J.; Lv, S.; Zhu, Z.; Li, Z. Vertically aligned MoS₂/ZnO nanowires nanostructures with highly enhanced NO₂ sensing activities. *Appl. Surf. Sci.* **2018**, *456*, 808–816. [[CrossRef](#)]
75. Liu, S.; Wang, Z.; Zhang, Y.; Dong, Z.; Zhang, T. Preparation of zinc oxide nanoparticle–reduced graphene oxide–gold nanoparticle hybrids for detection of NO₂. *RSC Adv.* **2015**, *5*, 91760–91765. [[CrossRef](#)]
76. Han, T.-H.; Bak, S.-Y.; Kim, S.; Lee, S.H.; Han, Y.-J.; Yi, M. Decoration of CuO NWs gas sensor with ZnO NPs for improving NO₂ sensing characteristics. *Sensors* **2021**, *21*, 2103. [[CrossRef](#)] [[PubMed](#)]
77. Kamble, V.S.; Zemase, R.K.; Gupta, R.H.; Aghav, B.D.; Shaikh, S.A.; Pawara, J.M.; Patil, S.K.; Salunkhe, S.T. Improved toxic NO₂ gas sensing response of Cu-doped ZnO thin-film sensors derived by simple co-precipitation route. *Opt. Mater.* **2022**, *131*, 112706. [[CrossRef](#)]
78. Şahin, Y.; Öztürk, S.; Kılınc, N.; Kösemen, A.; Erkovan, M.; Öztürk, Z.Z. Electrical conduction and NO₂ gas sensing properties of ZnO nanorods. *Appl. Surf. Sci.* **2014**, *303*, 90–96. [[CrossRef](#)]
79. Sun, K.; Zhan, G.; Zhang, L.; Wang, Z.; Lin, S. Highly sensitive NO₂ gas sensor based on ZnO nanoarray modulated by oxygen vacancy with Ce doping. *Sens. Actuators B Chem.* **2023**, *379*, 133294. [[CrossRef](#)]
80. Tian, H.; Fan, H.; Ma, J.; Liu, Z.; Ma, L.; Lei, S.; Fang, J.; Long, C. Pt-decorated zinc oxide nanorod arrays with graphitic carbon nitride nanosheets for highly efficient dual-functional gas sensing. *J. Hazard. Mater.* **2018**, *341*, 102–111. [[CrossRef](#)] [[PubMed](#)]

Disclaimer/Publisher’s Note: The statements, opinions and data contained in all publications are solely those of the individual author(s) and contributor(s) and not of MDPI and/or the editor(s). MDPI and/or the editor(s) disclaim responsibility for any injury to people or property resulting from any ideas, methods, instructions or products referred to in the content.